

# 1 Estimating vehicle carbon dioxide emissions from Boulder, Colorado using horizontal path-integrated 2 column measurements

3  
4 Eleanor M. Waxman<sup>1</sup>, Kevin C. Cossel<sup>1</sup>, Fabrizio Giorgetta<sup>1</sup>, Gar-Wing Truong<sup>1,2</sup>, William C. Swann<sup>1</sup>,  
5 Ian Coddington<sup>1</sup>, Nathan R. Newbury<sup>1</sup>

6  
7 <sup>1</sup>Applied Physics Division, NIST Boulder

8 <sup>2</sup>Now at: Crystalline Mirror Solutions  
9

## 10 Abstract

11 We performed seven and a half weeks of path-integrated concentration measurements of CO<sub>2</sub>, CH<sub>4</sub>, H<sub>2</sub>O,  
12 and HDO over the city of Boulder, Colorado. An open-path dual-comb spectrometer simultaneously  
13 measured time-resolved data across a reference path, located near the mountains to the west of the city, and  
14 across an over-city path that intersected two-thirds of the city, including two major commuter arteries. By  
15 comparing the measured concentrations over the two paths when the wind is primarily out of the west, we  
16 observe daytime CO<sub>2</sub> enhancements over the city. Given the warm weather and the measurement footprint,  
17 the dominant contribution to the CO<sub>2</sub> enhancement is from city vehicle traffic. We use a Gaussian plume  
18 model combined with reported city traffic patterns to estimate city emissions of on-road CO<sub>2</sub> as  $(6.2 \pm 2.2)$   
19  $\times 10^5$  metric tons (MT) CO<sub>2</sub>/year, after correcting for non-traffic sources. Within the uncertainty, this value  
20 agrees with the city bottom-up greenhouse gas inventory for the on-road vehicle sector of  $4.5 \times 10^5$  MT  
21 CO<sub>2</sub>/year. Finally, we discuss experimental modifications that could lead to improved estimates from our  
22 path-integrated measurements.  
23

## 24 1. Introduction

25 Measurements of greenhouse gases, especially CO<sub>2</sub> and CH<sub>4</sub>, are critical for monitoring,  
26 verification, and reporting as countries and cities work towards decreasing their carbon emissions.  
27 Measurements on the city-scale are critical because cities contribute to a large fraction of global  
28 emissions (Marcotullio et al., 2013; Seto et al., 2014). However, quantification of city greenhouse gas  
29 emissions is challenging, especially for CO<sub>2</sub> since it has a high background and numerous point and  
30 diffuse sources including traffic, power plants, and animal and plant respiration. Emissions of pollutants  
31 are typically determined using two methods: a top-down approach using atmospheric measurements over  
32 a specific site or area to adjust a prior model, and bottom-up inventories that calculate emissions based on  
33 sector activity and sector emissions factors. Here we demonstrate a technique for top-down  
34 measurements that uses an open-path sensor rather than a point sensor.

35 Quantification of CO<sub>2</sub> fluxes from cities has been determined from eddy covariance flux  
36 measurements with a point sensor located on a tower in or near a city (Nemitz et al., 2002; Velasco et al.,  
37 2005; Coutts et al., 2007; Bergeron and Strachan, 2011; Velasco et al., 2014). However, for a single  
38 sensor, the relatively small footprint of the eddy covariance flux measurements limits the utility of this  
39 technique for large cities as do violations of the horizontal homogeneity assumption (Järvi et al., 2018).  
40 To overcome this limitation, tower networks of point sensors can measure CO<sub>2</sub> at multiple sites within a  
41 city and at background sites outside the city (McKain et al., 2012; Lauvaux et al., 2013; Bréon et al.,  
42 2015; Staufer et al., 2016; Lauvaux et al., 2016; Shusterman et al., 2016; Mueller et al., 2017; Verhulst et  
43 al., 2017; Sargent et al., 2018; Mitchell et al., 2018). To distinguish the small enhancements compared to  
44 the large background, these networks often use expensive, high-precision cavity ringdown (CRDS)  
45 instruments resulting in a high cost. The BEACO<sub>2</sub>N network (Shusterman et al., 2016), on the other  
46 hand, has a much lower cost per sensor but requires significant calibration for quantitative results. All of  
47 these methods use an inversion to determine the total emissions and thus rely on well-known priors and  
48 high-resolution mesoscale atmospheric models.

49 More recently, several other approaches have also been applied to city-scale emissions. Aircraft  
50 mass balance measurements (White et al., 1976; Ryerson et al., 2001) have been used to determine city  
51 emissions (Mays et al., 2009; Heimbürger et al., 2017). However, the use of an aircraft is costly and labor

intensive, and therefore not suited to long-term continuous measurements. Column measurements from the Total Carbon Column Observation Network (TCCON) were used to calculate total South Coast Air Basin (SoCAB) CO and CH<sub>4</sub> emissions, but not CO<sub>2</sub> (Wunch et al., 2009). Data from the Orbiting Carbon Observatory satellite (OCO-2) was recently combined with TCCON data to estimate CO<sub>2</sub> emissions from the LA basin (Hedelius et al., 2018).

As an alternative to these approaches, horizontal, kilometer-scale, open-path instruments could in principle be used to determine CO<sub>2</sub> emissions from cities. Such instruments are capable of continuous measurements over a large area with a single instrument, e.g. (Wong et al., 2016; Dobler et al., 2017; Coburn et al., 2018). These sensors also have the advantage of being insensitive to small changes in local meteorology and are not subject to the same representation errors as point sensors (Ciais et al., 2010). Several such systems have been deployed. A laser absorption spectrometer system (GreenLITE) has mapped CO<sub>2</sub> concentrations over Paris, but not yet quantified emissions (Dobler et al., 2017). The California Laboratory of Atmospheric Remote Sensing Fourier Transform Spectrometer (CLARS-FTS) is a downward-looking slant column Fourier transform spectrometer (FTS) that scans across 28 measurement targets in the Los Angeles Basin to measure CO<sub>2</sub>, CH<sub>4</sub>, and O<sub>2</sub> (Wong et al., 2015). Based on the measured CH<sub>4</sub>:CO<sub>2</sub> ratio and the bottom-up CO<sub>2</sub> inventory from California Air Resources Board, researchers have calculated the LA Basin CH<sub>4</sub> emissions (Wong et al., 2016), but not yet the CO<sub>2</sub> emissions.

Here we present the quantification of city CO<sub>2</sub> emissions using open-path measurements made with a dual frequency comb spectrometer. While dual-comb spectroscopy is a relatively new technique it has a unique set of attributes that make it attractive for open path measurements (Rieker et al., 2014; Coddington et al., 2016; Waxman et al., 2017; Coburn et al., 2018). Dual-comb spectroscopy (DCS) is a high-resolution, broadband technique spanning hundreds of wavenumbers, but with a resolution that exceeds even high-end FTIRs leading to a negligible instrument lineshape. This allows for simultaneous measurements of multiple species and path-integrated temperature with low systematic uncertainty and without the need for instrument calibration. Additionally, the eye-safe, high-brightness, single transverse-mode output of a frequency comb allows for beam paths exceeding 10 km while the speed and parallelism of the measurement suppress any spectral distortion from the inevitable turbulence-induced power fluctuations over such a path.

Figure 1 shows the measurement layout for an initial campaign to quantify CO<sub>2</sub> emissions from Boulder, Colorado. Here we take the light from a dual comb spectrometer near the edge of the city and simultaneously measure two paths: a reference path that points west-southwest towards the mountains and an over-city path that crosses the city to the northeast, covering the main traffic arteries of the city with sensitivity to traffic emissions. We acquire time-resolved data at 5-minute resolution of CO<sub>2</sub>, CH<sub>4</sub>, H<sub>2</sub>O and isotopologues over 7.5 weeks. The dry mole fraction of CO<sub>2</sub> shows a diurnal cycle consistent with anthropogenic sources. In addition, there is a distinct difference between the weekday and weekend cycles for CO<sub>2</sub>, consistent with traffic patterns. In order to demonstrate the utility of this method for emissions quantification, we perform a preliminary estimate of the CO<sub>2</sub> emissions from traffic. To do this, we filter the data for days when the wind is out of the west and not too strong so that there is a measurable daytime enhancement in CO<sub>2</sub> between the reference path and over-city path. Given the weather, beam path location, and observation times, the dominant contribution will be from traffic rather than residential or industrial emissions. We apply a Gaussian plume model to calculate the city emissions based on the expected distributed source (due to traffic) and the path-averaged concentrations. After adjusting for small expected contributions from residential sources and a local utility plant, the measured emission value is scaled to annual city-wide emissions based on city traffic count data. We estimate  $(6.2 \pm 2.2) \times 10^5$  metric tons (MT) CO<sub>2</sub>/year, compared to the bottom-up City of Boulder inventory estimate of  $4.46 \times 10^5$  MT CO<sub>2</sub>/year. Finally, we discuss improvements to this estimate, which could be realized by more advantageous beam paths that sample a larger spatial and temporal fraction of the full city emissions and by a more detailed inventory model.

## 2. Experimental data

## 2.1 DCS measurements

The dual frequency comb spectroscopy (DCS) system was located on the top floor of the National Institute of Standards and Technology (NIST) building in Boulder, Colorado. This instrument has been described previously (Truong et al., 2016; Waxman et al., 2017). The light from the combs is split to generate two combined dual-comb outputs, one of which is transmitted over the reference path and one of which is transmitted over the city path (see Fig. 1.) Here, we transmit 2-10 mW of light spanning 1.561 to 1.656  $\mu\text{m}$ , which includes absorption lines from  $\text{CO}_2$ ,  $\text{CH}_4$ ,  $\text{H}_2\text{O}$  and  $\text{HDO}$ . The returning light from each path is detected and digitized to yield the transmitted optical spectrum at a point spacing of 0.0067  $\text{cm}^{-1}$  (1.5 picometer) and with effectively perfect (10 ppb) frequency accuracy and narrow instrument lineshape ( $\sim 4 \times 10^{-6} \text{ cm}^{-1}$ ). A typical spectrum from the reference path is shown in Fig. 2. A fit of this transmitted spectrum yields the path-averaged gas concentrations. The absolute frequency accuracy and high frequency resolution of the dual-comb spectrometers translates to a high precision and accuracy in the retrieved concentrations. Further, DCS spectra are undistorted by turbulence due to the simultaneous acquisition of all spectral channels and the fast sample rate of the instrument (1.6 ms/spectrum, averaged up to 5 minutes here) (Rieker et al., 2014).

In previous work (Waxman et al., 2017), we confirmed the high precision and accuracy possible with open-path DCS. Two DCS instruments, constructed by different teams, measured atmospheric air over adjacent paths over a two-week period. The retrieved path-averaged gas concentrations agreed to better than 0.6 ppm (0.14%) for  $\text{CO}_2$  and 7 ppb (0.35%) for  $\text{CH}_4$  across the full two week period, where the analysis of the two DCS instruments used a common spectral database (HITRAN 2008, Rothman et al., 2009) to retrieve the concentrations from the absorption spectrum. In the work here, a single DCS instrument probes the concentrations across two different open paths simultaneously, which should further suppress any systematic offsets to below 0.45 ppm (Waxman et al., 2017). In addition, (Waxman et al., 2017) compared the two DCS instruments to a stationary cavity ringdown (CRDS) point sensor whose inlet was approximately at the midpoint of the open path. This comparison actually took place over the reference path during the first two weeks of the present work. During that time, we found a roughly constant difference of 3.4 ppm  $\text{CO}_2$  and 17 ppb  $\text{CH}_4$  between the DCS and CRDS systems. At present, we attribute this offset to differences in the calibration scheme as the DCS is tied to the HITRAN database while the CRDS is tied to the manometric (or gravimetric depending on the gas) WMO scale. Similar level offsets have been observed in comparison of the TCCON open-path FTS instrument and point sensor-based vertical columns resulting in the TCCON  $\text{CO}_2$  scaling factor of 0.9898 (4.08 ppm for a mixing ratio of 400 ppm) (Wunch et al., 2015). This offset does not affect the results here as it is common to both the reference and over-city paths.

The reference and over-city paths had different path lengths and therefore used slightly different telescopes and launch powers. For the reference path, 2 mW of dual-comb light is launched from a 2-inch home-built off-axis telescope (Cossel et al., 2017; Waxman et al., 2017). The light travels to a 2.5-inch retroreflector located on a hilltop 1 km to the southwest of NIST and then is reflected back to a detector that is co-located with the launch telescope for a  $1950.17 \pm 0.15 \text{ m}$  round-trip path. Return powers vary constantly with air turbulence but we collect about 200  $\mu\text{W}$  for a typical 10 dB link loss. For the city path, 10 mW of dual-comb light is launched from a modified 10-inch diameter astronomical telescope to a 5-inch retroreflector located on a building roof 3.35 km to the northeast for a  $6730.66 \pm 0.15 \text{ m}$  round-trip path. We collect about 100  $\mu\text{W}$  for a typical 20 dB link loss. Round-trip path distances were measured with a laser range finder. Telescope tracking of the retroreflector is implemented to compensate for thermal drifts via a co-aligned 850 nm light emitting diode (LED) and Silicon CCD camera (Cossel et al., 2017; Waxman et al., 2017).

The measured spectra are analyzed as described in (Rieker et al., 2014; Waxman et al., 2017) at 32 second intervals. Briefly, we fit a 7<sup>th</sup>-order polynomial and HITRAN data to the measured spectrum in 100-GHz ( $0.333 \text{ cm}^{-1}$ ) sections to remove the underlying structure from the comb themselves (as opposed to the atmospheric absorption). We fit the resulting absorption spectrum twice: once in the region from

6171  $\text{cm}^{-1}$  to 6271  $\text{cm}^{-1}$  (1.595 to 1.620  $\mu\text{m}$ ) to obtain the path-averaged temperature from the 1.6  $\mu\text{m}$   $\text{CO}_2$  band, and once over the entire spectrum to obtain  $^{12}\text{CO}_2$ ,  $^{13}\text{CO}_2$ ,  $\text{CH}_4$ ,  $\text{H}_2\text{O}$ , and HDO concentrations using the retrieved temperature. We then use the retrieved  $\text{H}_2\text{O}$  concentration to correct the wet  $\text{CO}_2$  and  $\text{CH}_4$  mole fractions to dry mole fractions, hereafter referred to as  $X_{\text{CO}_2}$  and  $X_{\text{CH}_4}$  given in units of ppm and ppb (micromole of  $\text{CO}_2$  per mole of dry air, and nanomole of  $\text{CH}_4$  per mole of dry air). The correction equations are  $X_{\text{CO}_2} = \text{CO}_2/(1-\text{H}_2\text{O})$  and  $X_{\text{CH}_4} = \text{CH}_4/(1-\text{H}_2\text{O})$ .

The variations in the retrieved concentrations are due to statistical uncertainty, systematic uncertainty (discussed above), and the true variations in the gas concentrations. Figure 8 of (Waxman et al., 2017) quantified the statistical uncertainty in terms of the Allan deviation over the 2-km reference path for both  $X_{\text{CH}_4}$  and  $X_{\text{CO}_2}$ . Figure 3 here provides an Allan deviation for just  $X_{\text{CO}_2}$  over both the ~6.7-km city and ~2-km reference paths, as calculated from a relatively “flat” 1000-s period of this measurement campaign on the night of 3 to 4 October 2016. As expected, the statistical uncertainty over both paths improves as the square root of integration time until reaching a floor, which we attribute to real variations in the atmospheric gas concentrations. At 30 seconds, the statistical uncertainty of  $X_{\text{CO}_2}$  is 0.76 ppm for the reference path and 0.64 ppm for the over-city path, finally dropping to 0.21 ppm and 0.15 ppm, respectively, at about 15 minutes. In most subsequent figures, we show results at a 5-minute averaging time for which the statistical uncertainty is well under 0.3 ppm of  $X_{\text{CO}_2}$  for both paths and therefore well below the typical atmospheric variations. Note that the uncertainty also improves with path length, as expected due to the stronger absorption. The lower uncertainty over the city path reflects the expected improvement from the 3.4x longer path length lessened by the 2x reduction in return signal power for the longer path length.

## 2.2 Meteorological Measurements

Meteorological data including pressure, wind direction, and wind speed measurements are obtained from meteorological stations located at NCAR-Mesa and NCAR-Foothills (<ftp://ftp.eol.ucar.edu/pub/archive/weather>), which are approximately the endpoints of our measurement paths (see Fig. 1), as well as a 3-D sonic anemometer located at NIST. The path-averaged air temperature was retrieved from the  $\text{CO}_2$  spectra as described above.

## 2.3 Traffic data

We measure a subset of Boulder traffic, so we use the city traffic data to determine the fraction covered by our footprint (see Fig. 1). Traffic data from the City of Boulder is freely available at: [https://maps.bouldercolorado.gov/traffic-counts/?\\_ga=2.264109964.1414067815.1500302174-274759643.1492121882](https://maps.bouldercolorado.gov/traffic-counts/?_ga=2.264109964.1414067815.1500302174-274759643.1492121882). The city provides two types of traffic data that are useful in this work: the Arterial Count Program (ART) and the Turning Movement Count (TMC) data.

ART measures traffic at 18 major intersections in Boulder for five days (one work week, Monday through Friday) every year in one-hour bins to create a diurnal cycle. The traffic counts for 2016 are shown in Fig. 4. We use these data to scale our selected measurement time periods to a full day as discussed in section 3.3.4. Note that there is only a 10-20% “peak” in traffic counts at the standard commuter times with generally high traffic levels from 7:00 to ~19:00, which agrees with the traffic emissions reported by the Hestia inventory model for the similar city of Salt Lake City, UT (Mitchell et al., 2018).

TMC measures the number of vehicles at 140 intersections in Boulder for one work day per year during the hours of 7:45-8:45, 12:00-13:00, and 16:45-17:45. One third of each of these sites is measured every year. We have scaled the 2014 and 2015 data to 2016 traffic levels by using total vehicle mile values available from the City of Boulder. We approximate city vehicle emissions by using the TMC locations as our source locations with a source strength scaled based on the location’s fractional traffic count.

## 3 Results and Discussion

### 3.1 DCS measurements

All 7.5 weeks of DCS measurements of CO<sub>2</sub>, CH<sub>4</sub>, H<sub>2</sub>O, and HDO are shown in Fig. 5. HDO is not used here but is shown for completeness (note that the HDO concentration is scaled by the isotopic abundance in HITRAN). We have insufficient precision to measure time-resolved <sup>13</sup>CO<sub>2</sub> concentrations over the 2-km path. However, there are very clear enhancements in the over-city path relative to the reference path for the other trace gases, especially for CO<sub>2</sub>. These enhancements are observed primarily at night when the boundary layer is lower. For example, on Oct. 13 the CO<sub>2</sub> enhancement reaches 129 ppm and the CH<sub>4</sub> enhancement reaches 265 ppb. Daytime enhancements occur when the wind speed is very low and intermittent (typically below 5 m/s), which allows emitted gases to build up over the city. When the wind increases to steady moderate speeds, the concentrations drop quickly as the emissions are flushed out of the city. The H<sub>2</sub>O retrieval is important as accurate knowledge of the time-dependent water concentration is needed to calculate the dry CO<sub>2</sub> and CH<sub>4</sub> mole fractions (see Section 2.1). Also, the correlation of the water concentration between the two paths indicates the two paths sense the same air mass, which is further substantiated in Figure 7a and is central to attributing their different CO<sub>2</sub> concentration to local urban sources.

### 3.2 Diurnal Cycles

The diurnal cycle of X<sub>CO<sub>2</sub></sub> and X<sub>CH<sub>4</sub></sub> for both the reference path and the over city path are shown in Fig. 6 for weekdays (midnight to midnight Monday through Friday) and weekends (midnight to midnight Saturday and Sunday). We choose to include Monday as a weekday and Saturday as a weekend because the influence of emissions from the previous day is expected to be low. The diurnal cycle of the wind direction and the wind speed measured at NCAR Foothills are also shown in the top panel of Fig. 6. All diurnal cycles are the median values over the full 7.5 weeks of measurements and the bars reflect the 25%/75% quartile values.

The diurnal cycle of the reference path CO<sub>2</sub> is nearly flat and nearly identical for both weekends and weekdays. It has a slight maximum between 9 and 10 am, with average values of 410 to 420 ppm. The diurnal cycle of the city path CO<sub>2</sub> shows a different trend with a stronger diurnal variation. Overnight from about 6 pm (18:00) to 9 am, there is an enhancement in the CO<sub>2</sub> relative to the reference path as the CO<sub>2</sub> from the city sources builds up due to the low winds out of the west and a presumed collapsing nighttime boundary layer. During the weekdays, this enhancement increases in the morning consistent with the rise in traffic. After the morning, the combination of the presumed rising boundary layer, increased wind speed, and shift in average wind direction out of the west (270°) to the southeast (135 °) result in a drop in the city path CO<sub>2</sub>. Moreover, this shift in wind direction means that the reference path no longer samples the clean air from the direction of the mountains but rather sees a very similar CO<sub>2</sub> enhancement as the city path. (Fortunately, as discussed below, there are days when the wind does not shift direction so that there is a measured enhancement of the city path compared to the reference path.) In the early evening, as the wind speed drops and the wind direction shifts back to out of the west, the enhancement of the city path over the reference path reappears and continues overnight as the boundary layer presumably drops. In general, the CO<sub>2</sub> mixing ratios tend to be higher on the weekdays, sometimes exceeding 500 ppm, while weekend mixing ratios are entirely below 490 ppm. This difference is reflected in the median values as well, which reach about 440 ppm during the weekdays but only 430 ppm during the weekend.

The diurnal cycle of the reference path CH<sub>4</sub> is relatively flat for both weekends and weekdays at just over 1.9 ppm, with a slight peak between 9 and 10 am. The diurnal cycle of the city path CH<sub>4</sub> shows an enhancement, relative to the reference path, between midnight and about 9 am. We attribute this enhancement to sources of CH<sub>4</sub> within the city combined again with low nighttime winds and collapsing boundary layer. These sources may be leaking natural gas infrastructure such as observed in Boston (Phillips et al., 2013; McKain et al., 2015; Hendrick et al., 2016), Washington, D.C. (Jackson et al., 2014), and Indianapolis (Lamb et al., 2016). Unlike for CO<sub>2</sub>, the CH<sub>4</sub> diurnal cycle appears unrelated to traffic (nor would we expect it to be for clean-burning vehicles) as it does not increase during high traffic times.

### 3.3 Estimate for CO<sub>2</sub> emissions due to traffic

#### 3.3.1 Measurement day selections

To select test case days to estimate the city emissions, we filter the  $X_{CO_2}$  time series for time periods with daytime enhancement and a moderate wind strength predominantly out of the west (270 °). Given that the prevailing daytime winds are from the southeast (135°) and often strong, this limits the test case days significantly. However, as is clear from Fig. 1, for these wind conditions, the city path samples a significant fraction of the traffic emissions and the reference path samples no traffic emissions. We consider only daytime enhancements because the nighttime boundary layer behavior is significantly more complicated than a well-mixed daytime stable boundary layer. We find two days that meet these criteria: Saturday 22 October 2016 from 11:00 to 16:00. and Tuesday 25 October 2016 from 7:00 to 16:00. Both days have moderate wind speeds (on average, 5 m/s) as measured at both meteorological sites. There are additional days with daytime enhancement in  $X_{CO_2}$ , but the wind direction is variable. Additionally, there are many days with no daytime enhancement in  $X_{CO_2}$  because the high wind speeds (6 m/s or higher) prevented buildup of CO<sub>2</sub>. We use Oct. 22 as a proxy for all weekend days and Oct. 25 as a proxy for all weekdays. The  $X_{CO_2}$  and  $X_{CH_4}$  mixing ratios as well as wind speed and wind direction for these two case study days are shown in Fig. 7.

In order to confirm that the reference path measured clean background air and the over-city path measured city emissions, we calculated footprints for the two test case time periods using the Stochastic Time-Inverted Lagrangian Transport (STILT-R) model (Fasoli et al., 2018). The input meteorology file consisted of a uniform wind field with wind data from the NCAR Foothills lab, boundary layer height from the North American Regional Reanalysis (NARR), uniform turbulent velocity variance calculated from the Pasquill stability class (determined from wind speed and solar insolation) from the ground up to the boundary layer, and the hyper near-field scaling described in Fasoli et al., (2018). Average footprints for the two time periods are shown in Fig 7. The footprint for the reference path covers undeveloped areas extending from the near foothills into the mountains. The footprint for the over-city path also has contributions from the same general mountain region. In addition, this path has sensitivity to an extended area within the city and therefore to a large fraction of the traffic emissions. Note the open-path geometry leads to a much larger extended footprint for this path than would be the case for a single point sensor located at the same height within the city.

The variability in the reference CO<sub>2</sub> on both days is a real atmospheric effect. (In processing, any data is removed if the signal power is low, which is indicative of poor telescope alignment or strong weather-related attenuation over the beam path, so the variability is not due to variable signal strength.) We attribute this variability to the smaller footprint of the reference path relative to the over-city path, as seen in Fig. 7. If the CO<sub>2</sub> in the air is not fully mixed, then the temporal and spatial variability will be more evident in the path with the smaller footprint.

To convert from the measured enhancement to an emissions rate, we require a model that connects the source strength to the plume concentration. Since we do not have a high-resolution, spatially resolved inventory for Boulder similar to the Hestia model for Salt Lake City (Mitchell et al., 2018), we use the existing Boulder traffic inventory (see Section 2.3) in conjunction with a Gaussian plume model.

#### 3.3.2 Gaussian plume calculations

The standard Gaussian plume model that includes total reflection at the Earth's surface is (Seinfeld and Pandis, 2006):

$$c(x, y, z, t) = \frac{q}{2\pi\sigma_y\sigma_z u} \exp\left(-\frac{(y-y_0)^2}{2\sigma_y^2}\right) \left[ \exp\left(-\frac{(z-H)^2}{2\sigma_z^2}\right) + \exp\left(-\frac{(z+H)^2}{2\sigma_z^2}\right) \right] \quad (1)$$

where  $(x, y, z)$  is the location in space for which the plume concentration is being calculated,  $(x_0, y_0, H)$  is the emissions location,  $c(x, y, z)$  is the concentration at location  $(x, y, z)$  and time  $t$ ,  $q$  is the emissions strength

(usually in kg/s),  $\sigma_y$  and  $\sigma_z$  are the plume variances in the y and z direction as a function of travel distance and Pasquill stability class (Seinfeld and Pandis, 2006), and  $u$  is the wind speed in m/s. The wind is assumed to be in the x-direction. The plume variances are calculated as:

$$\sigma_y = \exp \left[ I_y + J_y (\ln \Delta x) + K_y (\ln \Delta x)^2 \right] \quad (2)$$

and

$$\sigma_z = \exp \left[ I_z + J_z (\ln \Delta x) + K_z (\ln \Delta x)^2 \right] \quad (3)$$

where  $I_y, J_y, K_y, I_z, J_z,$  and  $K_z$  are from a look-up table based on the Pasquill stability class, which depends on the wind speed and solar insolation (Seinfeld and Pandis, 2006) and  $\Delta x$  is the x-distance relative to the plume origin. This plume model does not include any reflection at the boundary layer height; however, due to the small spatial scales, this effect is negligible here.

We modify this equation in several ways: 1) Since we measure the column-integrated concentration over a finite beam path at an angle to the wind direction, we integrate the plume concentration along this beam path and then normalize to the length of the beam path. 2) We sum over the emissions locations in the city that contribute emissions to our measurements. Thus our overall measurement equation is:

$$(c - c_0) = \frac{Q}{L} \sum_{(x_j, y_j)} \int_0^L \frac{f_j}{2\pi\sigma_y\sigma_z u} \exp \left( \frac{-(s \sin \theta - y_j)^2}{2\sigma_y^2} \right) \left[ \exp \left( \frac{-(15 - s)^2}{2\sigma_z^2} \right) + \exp \left( \frac{-(15 + s)^2}{2\sigma_z^2} \right) \right] ds \quad (4)$$

where  $(c - c_0)$  is our path-integrated concentration enhancement measurement (in MT/m<sup>3</sup> and MT is metric tons; 1 MT = 1000 kg) along our path  $s$  which goes from 0 to  $L$ ,  $Q$  is the total city emissions in MT/hour,  $L$  is our path length in m,  $(x_j, y_j)$  are the source emissions locations,  $f_j$  is the fraction of traffic at source location  $(x_j, y_j)$  relative to traffic over all locations in the city from the TMC database,  $u$  is the wind speed in m/s,  $\theta$  is the angle of the beam path with respect to the wind direction, and  $\sigma_y$  and  $\sigma_z$  are the plume dispersions in m in the y and z directions, which depend on the sources distance from the beam path. In writing (4), we assume the wind is in the  $+\hat{x}$  direction (which assumption is relaxed below). We assume that all plume emission locations are vehicle tailpipes at 1 m above the ground, and the beam path runs 15 m above ground so all measurement heights are at 15 m above ground.

#### Grid rotation for variable wind directions

To calculate (4), we grid the emissions locations using UTM (Universal Transverse Mercator) coordinates obtained from Google Earth, where we then define north as  $+\hat{y}$  and east as  $+\hat{x}$ . We translate the coordinate system such that the DCS path begins at the origin (0,0) and travels a distance  $L$  at angle  $\theta$  with respect to the x-axis. Eq. (4) is then valid provided the wind is directly in the  $+\hat{x}$  direction. More generally, the wind is at a time varying small angle  $\phi(t)$  with respect to  $+\hat{x}$ . Therefore, we apply a rotation about the origin (Prussin et al., 2015):

$$\begin{bmatrix} \cos \phi & \sin \phi \\ -\sin \phi & \cos \phi \end{bmatrix} \begin{bmatrix} x \\ y \end{bmatrix} = \begin{bmatrix} x' \\ y' \end{bmatrix}$$

to generate new traffic coordinates  $(x'_j, y'_j)$  and a new parameterized DCS beam path of  $(s \cos(\theta'), s \sin(\theta'))$  where  $\theta' = \theta - \phi(t)$ . In this new coordinate system, the wind is along the  $+\hat{x}$  direction and Eq. (4) holds with the substitutions  $\theta \rightarrow \theta'$  and  $y_j \rightarrow y'_j$ , and where the  $\sigma_y$  and  $\sigma_z$  are calculated based on the distance  $\Delta x = |x'_j - (y'_j / \tan \theta')|$ .

#### Time dependent estimate of $Q(t)$

The rotated Eq. (4) can be solved for  $Q$  in terms of the measured or estimated values of  $c(t) - c_0(t)$ ,  $u(t)$ ,  $\Delta \phi(t)$ ,  $\sigma_y(t)$ ,  $\sigma_z(t)$ ,  $\theta$ ,  $L$ , and  $f_i$ , where the first five quantities are time dependent. The resulting, time-dependent  $Q(t)$  for each test case day is shown in the bottom panels of Fig. 7 and has a mean value and

standard deviation of  $Q_{\text{Oct22}} = 31 \pm 17$  MT CO<sub>2</sub>/hour for October 22 and  $Q_{\text{Oct25}} = 165 \pm 45$  MT CO<sub>2</sub>/hour for October 25 for the 5-minute averaged data as shown.

#### *Uncertainty in $Q(t)$*

Seven measured parameters factor in to the emissions calculation of  $Q(t)$  for the two days. These are given in Table I along with the instrumental measurement precision and the observed variability. Note that solar insolation is used solely in the determination of the Pasquill stability class (Seinfeld and Pandis, 2006). The stability class is relatively insensitive to the variations in solar insolation observed on the two test case days. As can be seen in the table, the uncertainty is dominated by the natural variability in parameters like wind speed, wind direction, and CO<sub>2</sub> concentration rather than the DCS spectrometer precision. The observed variability over the 5-9 hour period is typically at least a factor of 2 larger than the instrument precision. The variability in these parameters leads to the observed variability in  $Q(t)$ . We use the mean of  $Q(t)$  as our emissions value and the standard deviation (at 5-minute time-averaging) as its uncertainty. In using this standard deviation as a measure of the uncertainty, we attempt to capture the uncertainty associated with the discrepancies between, for example, the weather-station measurements of wind direction and speed relative to the true wind direction (which results in greater or fewer number of plumes from the given traffic locations intercepting the measurement path). This variability appears in  $Q(t)$  as the nominal measured wind direction varies. Future systems with redundant, distributed DCS beam paths would provide a superior estimate of all these uncertainties.

In addition, there are assumptions, and possible uncertainties, inherent to the Gaussian plume model. First, the model does not include the effects of buildings, trees, or other objects that could break up the plume between the emissions location and the beam path. Second, we assume that all CO<sub>2</sub> emissions come from the discrete locations shown in Fig. 1, while in reality the emissions are likely substantially more diffuse. The assumption of discrete emissions simplifies modeling and is feasible due to the city traffic data but may result in a bias due to the coarse distribution of traffic measurements. Third, we approximate the measurement height at 15 m above ground although the beam height differs over the path since Boulder is not perfectly flat. Finally, we use standard  $I_y$ ,  $J_y$ ,  $K_y$ ,  $I_z$ ,  $J_z$ , and  $K_z$  values which were derived for rural areas (Turner, 1970) which may be different than urban or suburban areas. However, the greatest differences between rural and urban conditions are expected to be at night (Turner, 1970).

#### 3.3.3 Corrections for non-traffic sources of CO<sub>2</sub>

There are a number of non-traffic sources of CO<sub>2</sub> that could contribute to our measured  $X_{\text{CO}_2}$  enhancement including local power plants, residential emission, and biological activity. These non-traffic source should have relatively minor contribution for several reasons. First, the footprint of the over-city path does not overlap the large power plant to the east of the Boulder city limits. Second, the temperature during the two test case days was 24 °C and 20 °C (68 °F and 75 °F) on October 22 and 25th leading to minimal residential and commercial heating. Third, the measurements occurred in October after leaf senescence so there should be negligible biological activity. Nevertheless, as discussed below, we do adjust our measurements to account for the relatively minor contribution from non-traffic sources before scaling up to an estimate of the annual traffic emissions.

We first consider power plants. There are two power generation facilities on the Department of Commerce (DOC) campus located near the NIST building that houses the dual-comb spectrometer: the site's Central Utilities Plant (CUP), and the National Oceanic and Atmospheric Administration (NOAA) building's boilers. To calculate their average CO<sub>2</sub> emissions, we used available fuel consumption data (October 2016 monthly average for the CUP and mid-November to mid-December 2016 average for the NOAA boilers; October data was unavailable) and the EPA emissions factor (EPA, 1995). We then modeled the CUP and boiler plume emissions using WindTrax (Flesch et al., 1995, 2004) with wind speed and direction data from the NCAR-Mesa site. We find that due to the moderate wind speeds (~5 m/s) during our case study days and the height mismatch between the emission stacks and our measurement path over the DOC campus, there is negligible enhancement over the reference path. Given



the location of the emission sources and the wind direction during our measurement periods, the emissions also do not cross the over-city beam path. Therefore, we apply no correction for these two power plant emissions.

The University of Colorado also has a power plant that falls within the main footprint associated with the over-city beam path, shown in Fig. 7a, and whose emissions are expected to intersect our over-city beam path. The EPA Greenhouse Gas Reporting Program (GHGRP, <https://www.epa.gov/ghgreporting>) lists the 2017 emission from the power plant as  $2.7 \times 10^4$  MT CO<sub>2</sub> or an average of 3.1 MT/hour. (No breakdown by season or hour is provided.) We apply this correction to our previous daily values and add a conservative uncertainty equal to this correction in quadrature with the previous uncertainty. The new adjusted values are then  $28 \pm 17$  MT CO<sub>2</sub>/hour for October 22 and  $162 \pm 45$  MT CO<sub>2</sub>/hour for October 25.

The large Valmont power station lies just outside the city limits to the east of Boulder; however, given its location and the dominant westerly wind, emissions from this source does not reach our beam paths. There are no other power generation facilities within the city that report to the GHGRP, so we make no further corrections based on power plants.

In addition, there are also likely diffuse emissions from residential and commercial furnaces and water heaters that use natural gas. The City of Boulder Community Greenhouse Gas Emissions Inventory reports twenty percent of the city emissions, or  $3.18 \times 10^5$  MT CO<sub>2</sub>e, were from natural gas in 2016 ([https://www-static.bouldercolorado.gov/docs/2016\\_Greenhouse\\_Gas\\_Emissions\\_Inventory\\_Report\\_FINAL-1-201803121328.pdf?\\_ga=2.130927943.970967930.1525795820-107394975](https://www-static.bouldercolorado.gov/docs/2016_Greenhouse_Gas_Emissions_Inventory_Report_FINAL-1-201803121328.pdf?_ga=2.130927943.970967930.1525795820-107394975)). The natural gas usage varies strongly by month with building heating requirements. Although our measurements occurred in October, the measurement days were quite warm (20-24 C) so that residential and commercial building heating was unlikely and the use of an annual average would overestimate any contribution. Instead, we scale the natural gas usage according to the monthly breakdown provided by the United States Energy Information Administration database for Colorado (<https://www.eia.gov/dnav/ng/hist/n3010co2m.htm>). The mean daytime (approximately sunrise to sunset, 7 am to 6 pm) temperature in October was 18.2 C while the mean temperature (including day and night) for October was 15.7 C. Our daytime-only measurements therefore had a mean temperature that was much closer to the mean temperature (day and night) of September, which was 19.2 C. Therefore, we scale the Boulder annual natural gas consumption by the September 2016 natural gas usage, which was 2.4% of the Colorado annual total according (<https://www.eia.gov/dnav/ng/hist/n3010co2m.htm>). The estimated total emissions from residential and commercial natural gas usage in Boulder over our measurement days is then 10.2 MT CO<sub>2</sub>/hour. We apply this correction to our measured values and include a (conservative) uncertainty equal to this correction. The new adjusted values are then  $Q_{\text{Oct22,adj}} = 18 \pm 20$  MT CO<sub>2</sub>/hour for October 22 and  $Q_{\text{Oct25,adj}} = 152 \pm 46$  MT CO<sub>2</sub>/hour for October 25.

Once leaf senescence has completed, neither plants nor soil respiration contribute to CO<sub>2</sub> signal (Matyssek et al., 2013). The National Phenology Network (USA National Phenology Network, 2018) data shows that for the site nearest to Boulder (64 km north of Boulder), the leaf fall dates were September 15, 2016 for box elder trees October 6, 2016 for Eastern cottonwoods. Thus by our measurement dates leaf senescence should be fully complete and plants will not contribute to the city CO<sub>2</sub> enhancement. We note that a wide range of biogenic contributions to CO<sub>2</sub> have been noted in the literature (Gurney et al., 2017; Mitchell et al., 2018; Sargent et al., 2018).

### 3.3.4 Scaling to annual emissions

In order to compare with the city inventory, we scale our results to an annual total. To do this, we use the hourly traffic data of Fig. 4 to scale  $Q_{\text{Oct22,adj}}$  and  $Q_{\text{Oct25,adj}}$  to a daily emission. Based on Figure 4, 34% of the total traffic counts occur during the 5-hour measurement period on Oct. 22 and 52% of the total traffic counts occur during the 8-hour measurement period on Oct. 25 (excluding the 13:00 to 14:00 period). The daily emissions are then  $Q_{\text{Oct22,day}} = Q_{\text{Oct22,adj}} \times (5 \text{ hours}) \div (0.34)$  and  $Q_{\text{Oct25,day}} = Q_{\text{Oct25,adj}} \times (8 \text{ hours}) \div (0.52)$  (The traffic data in Fig. 4 is based on weekday measurement and we assume that the

hourly distribution is the same for weekends; this may lead to a slight overestimate in the weekend data where a larger fraction of emissions occurs between 11 am and 4 pm than on weekdays.) We then scale to annual emissions by assuming that the emissions on Oct. 22 are representative of all 112 weekend/holiday days and the emissions on Oct. 25 are representative of all 253 workdays. Including their uncertainty, this calculation yields  $(6.2 \pm 1.8) \times 10^5$  MT CO<sub>2</sub>/year.

The scaling relies heavily on the traffic count data supplied by the city of Boulder, which does not have an associated uncertainty value. A comparison of these data over several years shows a typical 7% statistical variation at a given TMC location, after removing a linear trend. We assume this reflects day-to-day fluctuations in traffic. In addition, there will be seasonal variations, which is not captured in the extrapolation from our two test case days to the annual emissions. Due to the lack of seasonal data for Boulder traffic, we use the detailed Hestia traffic inventory for Salt Lake City, UT given in Figure 2 of (Mitchell et al., 2018). These data show a variation of  $\pm 18\%$  in traffic emissions between “summer” and “winter” months. Combined in quadrature with the 7% statistical uncertainty in the TMC traffic count data, this leads to an additional  $\sim 20\%$  uncertainty to the scaled annual estimate. As noted earlier, we have not applied any additional uncertainty on the reliance on the TMC data as a proxy for emissions locations.

Including the additional uncertainty on the scaling to annual emissions, we estimate an annual emission rate of  $(6.2 \pm 2.2) \times 10^5$  MT CO<sub>2</sub>/year for traffic carbon emissions for Boulder CO.

#### 4 Comparison with city estimates

The city vehicle emissions estimate comes from total vehicle miles traveled based on data from the transportation department, miles per gallon inputs from the EPA state inventory tool, and vehicle type distribution from the Colorado Department of Public Health and the Environment (Kimberlee Rankin, City of Boulder, personal communication). The City of Boulder estimates total vehicle emissions of  $4.50 \times 10^5$  metric tons (MT) of CO<sub>2</sub> in 2016 ([https://www-static.bouldercolorado.gov/docs/2016\\_Greenhouse\\_Gas\\_Emissions\\_Inventory\\_Report\\_FINAL-1-201803121328.pdf?\\_ga=2.130927943.970967930.1525795820-107394975](https://www-static.bouldercolorado.gov/docs/2016_Greenhouse_Gas_Emissions_Inventory_Report_FINAL-1-201803121328.pdf?_ga=2.130927943.970967930.1525795820-107394975)). On-road emissions account for greater than 99% of the transportation emissions, so we have scaled this value down by one percent for an on-road emissions value of  $4.46 \times 10^5$  MT CO<sub>2</sub>. We assume that all traffic emissions are CO<sub>2</sub> rather than a mix of CO<sub>2</sub> and CH<sub>4</sub>. There is no uncertainty provided by the city on this value.

In comparison, we estimate  $(6.2 \pm 2.2) \times 10^5$  MT CO<sub>2</sub>/year, which is 139% of the city estimate but agrees within the given uncertainty. Interestingly, other studies have also found that emissions measurements were higher than the reported inventory values. Brioude et al., (2013) found top-down aircraft estimates of Los Angeles county and the South Coast Air Basin (SoCAB) CO<sub>2</sub> were 1.45 times larger than the Vulcan 2005 inventory (Gurney et al., 2009). An earlier aircraft campaign over Sacramento, CA found an average CO<sub>2</sub> emission, with 100% uncertainty, that was 15-20% higher than the Vulcan estimate (Turnbull et al., 2011). Lauvaux et al. (2016) compared Indianapolis city CO<sub>2</sub> emissions measured by a network of CRDS instruments to the HESTIA inventory (Gurney et al., 2012) during INFLUX (Davis et al., 2017). They found that despite the building-scale resolution in the HESTIA inventory, it still under-estimated the annual CO<sub>2</sub> flux by 20%. An updated version of HESTIA predicted very similar emissions estimates for on-road, residential, and commercial sectors, so the discrepancy was attributed to missing sources of CO<sub>2</sub>, including animal (primarily human and companion animal) respiration, biofuel combustion, and biosphere respiration (Gurney et al., 2017).

##### 4.1 Improvements in future measurements

Future improvements should include additional and different beam paths, selected based on prevailing wind directions. (Our initial assumption that the mountain path would generally act as a reference path was incorrect since the prevailing daytime winds are not out of the west but rather the southeast.) An east-west running beam north of the city and one south of the city would allow us to utilize a larger fraction of the data as the predominant midday wind direction during the fall is out of the north to north-east (see Fig. 1). Even longer beam paths would also interrogate a larger fraction of the city and measure a correspondingly larger fraction of the vehicle emissions. Vertically-resolved data from e.g. a

series of stacked retroreflectors would better test the assumption of vertically-dispersing Gaussian plumes.

Additionally, more extensive modeling to cover variable wind directions and speeds would allow the incorporation of a much larger fraction of the data than the two days selected here. An inversion-based model similar to (Lauvaux et al., 2013) could potentially be applied to a small city like Boulder; however this would depend heavily on the quality of the bottom-up emissions inventory used to generate the priors. Indeed, one of the major future improvements would be to generate a detailed Hestia inventory of Boulder, CO similar to that generated for Salt Lake City, UT (Mitchell et al., 2018).

## 5 Conclusions

We demonstrate the use of an open-path dual frequency comb spectroscopy system for quantifying city emissions of carbon dioxide. We send light over two paths: a reference path that samples the concentration of gases entering the city from the west, and an over-city path that measures the concentrations of gases after the air mass has crossed approximately two-thirds of the city including two major commuter arteries. The measured diurnal cycle shows a significant traffic-related enhancement in the carbon dioxide signal during weekdays in the over-city path compared to the reference path. We select two case study days with appropriate wind conditions and apply Gaussian plume modeling to estimate the total vehicular carbon emission. We then scale these results up to annual city-wide emissions using traffic data from the City of Boulder. We find overall traffic related carbon emissions that are approximately 1.4 times greater than the city's bottom-up traffic emissions inventory but with an uncertainty that encompasses the city inventory estimate. Further improvements to this method should include improved design of reference and over-city paths and a more detailed inventory model for Boulder CO, which together should further reduce the overall uncertainty in the estimate.

Acknowledgements: We thank Kimberlee Rankin, Randall Rutsch, Bill Covern, and Chris Hagelin from the City of Boulder for city inventory and traffic information and Dave Plusquellic and Caroline Alden for assistance with the manuscript. This work was funded by Defense Advanced Research Program Agency DSO SCOUT program, and James Whetstone and the NIST special program office. Eleanor M. Waxman and Kevin C. Cossel are partially supported by National Research Council postdoctoral fellowships.

## 5. References

Bergeron, O. and Strachan, I. B.: CO<sub>2</sub> sources and sinks in urban and suburban areas of a northern mid-latitude city, *Atmos. Environ.*, 45(8), 1564–1573, doi:10.1016/j.atmosenv.2010.12.043, 2011.

Bréon, F. M., Broquet, G., Puygrenier, V., Chevallier, F., Xueref-Remy, I., Ramonet, M., Dieudonné, E., Lopez, M., Schmidt, M., Perrussel, O. and Ciais, P.: An attempt at estimating Paris area CO<sub>2</sub> emissions from atmospheric concentration measurements, *Atmos Chem Phys*, 15(4), 1707–1724, doi:10.5194/acp-15-1707-2015, 2015.

Brioude, J., Angevine, W. M., Ahmadov, R., Kim, S.-W., Evan, S., McKeen, S. A., Hsie, E.-Y., Frost, G. J., Neuman, J. A., Pollack, I. B., Peischl, J., Ryerson, T. B., Holloway, J., Brown, S. S., Nowak, J. B., Roberts, J. M., Wofsy, S. C., Santoni, G. W., Oda, T. and Trainer, M.: Top-down estimate of surface flux in the Los Angeles Basin using a mesoscale inverse modeling technique: assessing anthropogenic emissions of CO, NO<sub>x</sub> and CO<sub>2</sub> and their impacts, *Atmos Chem Phys*, 13(7), 3661–3677, doi:10.5194/acp-13-3661-2013, 2013.

Ciais, P., Rayner, P., Chevallier, F., Bousquet, P., Logan, M., Peylin, P. and Ramonet, M.: Atmospheric inversions for estimating CO<sub>2</sub> fluxes: methods and perspectives, *Clim. Change*, 103(1–2), 69–92, doi:10.1007/s10584-010-9909-3, 2010.

546 Coburn, S., Alden, C. B., Wright, R., Cossel, K., Baumann, E., Truong, G.-W., Giorgetta, F., Sweeney,  
547 C., Newbury, N. R., Prasad, K., Coddington, I. and Rieker, G. B.: Regional trace-gas source attribution  
548 using a field-deployed dual frequency comb spectrometer, *Optica*, 5(4), 320–327,  
549 doi:10.1364/OPTICA.5.000320, 2018.

550 Coddington, I., Newbury, N. and Swann, W.: Dual-comb spectroscopy, *Optica*, 3(4), 414,  
551 doi:10.1364/OPTICA.3.000414, 2016.

552 Cossel, K. C., Waxman, E. M., Giorgetta, F. R., Cermak, M., Coddington, I. R., Hesselius, D., Ruben, S.,  
553 Swann, W. C., Truong, G.-W., Rieker, G. B. and Newbury, N. R.: Open-path dual-comb spectroscopy to  
554 an airborne retroreflector, *Optica*, 4(7), 724–728, doi:10.1364/OPTICA.4.000724, 2017.

555 Coutts, A. M., Beringer, J. and Tapper, N. J.: Characteristics influencing the variability of urban CO<sub>2</sub>  
556 fluxes in Melbourne, Australia, *Atmos. Environ.*, 41(1), 51–62, doi:10.1016/j.atmosenv.2006.08.030,  
557 2007.

558 Davis, K. J., Deng, A., Lauvaux, T., Miles, N. L., Richardson, S. J., Sarmiento, D. P., Gurney, K. R.,  
559 Hardesty, R. M., Bonin, T. A., Brewer, W. A., Lamb, B. K., Shepson, P. B., Harvey, R. M., Cambaliza,  
560 M. O., Sweeney, C., Turnbull, J. C., Whetstone, J. and Karion, A.: The Indianapolis Flux Experiment  
561 (INFLUX): A test-bed for developing urban greenhouse gas emission measurements, *Elem Sci Anth*,  
562 5(0), 21, doi:10.1525/elementa.188, 2017.

563 Dobler, J. T., Zaccheo, T. S., Pernini, T. G., Blume, N., Broquet, G., Vogel, F., Ramonet, M., Braun, M.,  
564 Stauffer, J., Ciais, P. and Botos, C.: Demonstration of spatial greenhouse gas mapping using laser  
565 absorption spectrometers on local scales, *J. Appl. Remote Sens.*, 11(1), 014002,  
566 doi:10.1117/1.JRS.11.014002, 2017.

567 EPA: AP 42, Fifth Edition Compilation of Air Pollutant Emissions Factors, Volume 1: Stationary Point  
568 and Area Sources, [online] Available from: [https://www.epa.gov/air-emissions-factors-and-](https://www.epa.gov/air-emissions-factors-and-quantification/ap-42-compilation-air-emission-factors#5thed)  
569 [quantification/ap-42-compilation-air-emission-factors#5thed](https://www.epa.gov/air-emissions-factors-and-quantification/ap-42-compilation-air-emission-factors#5thed), 1995.

570 Fasoli, B., Lin, J. C., Bowling, D. R., Mitchell, L. and Mendoza, D.: Simulating atmospheric tracer  
571 concentrations for spatially distributed receptors: updates to the Stochastic Time-Inverted Lagrangian  
572 Transport model's R interface (STILT-R version 2), *Geosci. Model Dev.*, 11(7), 2813–2824,  
573 doi:<https://doi.org/10.5194/gmd-11-2813-2018>, 2018.

574 Flesch, T. K., Wilson, J. D. and Yee, E.: Backward-Time Lagrangian Stochastic Dispersion Models and  
575 Their Application to Estimate Gaseous Emissions, *J. Appl. Meteorol.*, 34(6), 1320–1332,  
576 doi:10.1175/1520-0450(1995)034<1320:BTLSDM>2.0.CO;2, 1995.

577 Flesch, T. K., Wilson, J. D., Harper, L. A., Crenna, B. P. and Sharpe, R. R.: Deducing Ground-to-Air  
578 Emissions from Observed Trace Gas Concentrations: A Field Trial, *J. Appl. Meteorol.*, 43(3), 487–502,  
579 doi:10.1175/1520-0450(2004)043<0487:DGEFOT>2.0.CO;2, 2004.

580 Gurney, K. R., Mendoza, D. L., Zhou, Y., Fischer, M. L., Miller, C. C., Geethakumar, S. and Du Can, S.  
581 D. L. R.: High Resolution Fossil Fuel Combustion CO<sub>2</sub> Emission Fluxes for the United States, *Environ.*  
582 *Sci. Technol.*, 43(14), 5535–5541, doi:10.1021/es900806c, 2009.

583 Gurney, K. R., Razlivanov, I., Song, Y., Zhou, Y., Benes, B. and Abdul-Massih, M.: Quantification of  
584 Fossil Fuel CO<sub>2</sub> Emissions on the Building/Street Scale for a Large U.S. City, *Environ. Sci. Technol.*,  
585 46(21), 12194–12202, doi:10.1021/es3011282, 2012.

586 Gurney, K. R., Liang, J., Patarasuk, R., O’Keeffe, D., Huang, J., Hutchins, M., Lauvaux, T., Turnbull, J.  
587 C. and Shepson, P. B.: Reconciling the differences between a bottom-up and inverse-estimated FFCO<sub>2</sub>  
588 emissions estimate in a large US urban area, *Elem Sci Anth*, 5(0), doi:10.1525/elementa.137, 2017.

589 Hedelius, J. K., Liu, J., Oda, T., Maksyutov, S., Roehl, C. M., Iraci, L. T., Podolske, J. R., Hillyard, P.  
590 W., Liang, J., Gurney, K. R., Wunch, D. and Wennberg, P. O.: Southern California megacity CO<sub>2</sub>, CH<sub>4</sub>,  
591 and CO flux estimates using ground- and space-based remote sensing and a Lagrangian model,  
592 *Atmospheric Chem. Phys.*, 18(22), 16271–16291, doi:https://doi.org/10.5194/acp-18-16271-2018, 2018.

593 Heimbürger, A. M. F., Harvey, R. M., Shepson, P. B., Stirm, B. H., Gore, C., Turnbull, J., Cambaliza, M.  
594 O. L., Salmon, O. E., Kerlo, A.-E. M., Lavoie, T. N., Davis, K. J., Lauvaux, T., Karion, A., Sweeney, C.,  
595 Brewer, W. A., Hardesty, R. M. and Gurney, K. R.: Assessing the optimized precision of the aircraft mass  
596 balance method for measurement of urban greenhouse gas emission rates through averaging, *Elem Sci*  
597 *Anth*, 5(0), doi:10.1525/elementa.134, 2017.

598 Hendrick, M. F., Ackley, R., Sanaie-Movahed, B., Tang, X. and Phillips, N. G.: Fugitive methane  
599 emissions from leak-prone natural gas distribution infrastructure in urban environments, *Environ. Pollut.*,  
600 213, 710–716, doi:10.1016/j.envpol.2016.01.094, 2016.

601 Jackson, R. B., Down, A., Phillips, N. G., Ackley, R. C., Cook, C. W., Plata, D. L. and Zhao, K.: Natural  
602 Gas Pipeline Leaks Across Washington, DC, *Environ. Sci. Technol.*, 48(3), 2051–2058,  
603 doi:10.1021/es404474x, 2014.

604 Järvi, L., Rannik, Ü., Kokkonen, T. V., Kurppa, M., Karppinen, A., Kouznetsov, R. D., Rantala, P.,  
605 Vesala, T. and Wood, C. R.: Uncertainty of eddy covariance flux measurements over an urban area based  
606 on two towers, *Atmospheric Meas. Tech.*, 11(10), 5421–5438, doi:https://doi.org/10.5194/amt-11-5421-  
607 2018, 2018.

608 Lamb, B. K., Cambaliza, M. O. L., Davis, K. J., Edburg, S. L., Ferrara, T. W., Floerchinger, C.,  
609 Heimbürger, A. M. F., Herndon, S., Lauvaux, T., Lavoie, T., Lyon, D. R., Miles, N., Prasad, K. R.,  
610 Richardson, S., Roscioli, J. R., Salmon, O. E., Shepson, P. B., Stirm, B. H. and Whetstone, J.: Direct and  
611 Indirect Measurements and Modeling of Methane Emissions in Indianapolis, Indiana, *Environ. Sci.*  
612 *Technol.*, 50(16), 8910–8917, doi:10.1021/acs.est.6b01198, 2016.

613 Lauvaux, T., Miles, N. L., Richardson, S. J., Deng, A., Stauffer, D. R., Davis, K. J., Jacobson, G., Rella,  
614 C., Calonder, G.-P. and DeCola, P. L.: Urban Emissions of CO<sub>2</sub> from Davos, Switzerland: The First Real-  
615 Time Monitoring System Using an Atmospheric Inversion Technique, *J. Appl. Meteorol. Climatol.*,  
616 52(12), 2654–2668, doi:10.1175/JAMC-D-13-038.1, 2013.

617 Lauvaux, T., Miles, N. L., Deng, A., Richardson, S. J., Cambaliza, M. O., Davis, K. J., Gaudet, B.,  
618 Gurney, K. R., Huang, J., O’Keeffe, D., Song, Y., Karion, A., Oda, T., Patarasuk, R., Razlivanov, I.,  
619 Sarmiento, D., Shepson, P., Sweeney, C., Turnbull, J. and Wu, K.: High-resolution atmospheric inversion  
620 of urban CO<sub>2</sub> emissions during the dormant season of the Indianapolis Flux Experiment (INFLUX), *J.*  
621 *Geophys. Res. Atmospheres*, 121(10), 2015JD024473, doi:10.1002/2015JD024473, 2016.

622 Marcotullio, P. J., Sarzynski, A., Albrecht, J., Schulz, N. and Garcia, J.: The geography of global urban  
623 greenhouse gas emissions: an exploratory analysis, *Clim. Change*, 121(4), 621–634, doi:10.1007/s10584-  
624 013-0977-z, 2013.

625 Matyssek, R., Clarke, N., Cudlin, P., Mikkelsen, T. N., Tuovinen, J.-P., Wieser, G. and Paoletti, E.:  
626 Climate Change, Air Pollution and Global Challenges: Understanding and Perspectives from Forest

627 Research, Elsevier, London, UNITED KINGDOM. [online] Available from:  
628 <http://ebookcentral.proquest.com/lib/noaalabs-ebooks/detail.action?docID=1568332> (Accessed 19  
629 December 2018), 2013.

630 Mays, K. L., Shepson, P. B., Stirm, B. H., Karion, A., Sweeney, C. and Gurney, K. R.: Aircraft-Based  
631 Measurements of the Carbon Footprint of Indianapolis, *Environ. Sci. Technol.*, 43(20), 7816–7823,  
632 doi:10.1021/es901326b, 2009.

633 McKain, K., Wofsy, S. C., Nehrkorn, T., Eluszkiewicz, J., Ehleringer, J. R. and Stephens, B. B.:  
634 Assessment of ground-based atmospheric observations for verification of greenhouse gas emissions from  
635 an urban region, *Proc. Natl. Acad. Sci.*, 109(22), 8423–8428, doi:10.1073/pnas.1116645109, 2012.

636 McKain, K., Down, A., Raciti, S. M., Budney, J., Hutyra, L. R., Floerchinger, C., Herndon, S. C.,  
637 Nehrkorn, T., Zahniser, M. S., Jackson, R. B., Phillips, N. and Wofsy, S. C.: Methane emissions from  
638 natural gas infrastructure and use in the urban region of Boston, Massachusetts, *Proc. Natl. Acad. Sci.*,  
639 112(7), 1941–1946, doi:10.1073/pnas.1416261112, 2015.

640 Mitchell, L. E., Lin, J. C., Bowling, D. R., Pataki, D. E., Strong, C., Schauer, A. J., Bares, R., Bush, S. E.,  
641 Stephens, B. B., Mendoza, D., Mallia, D., Holland, L., Gurney, K. R. and Ehleringer, J. R.: Long-term  
642 urban carbon dioxide observations reveal spatial and temporal dynamics related to urban characteristics  
643 and growth, *Proc. Natl. Acad. Sci.*, 115(12), 2912–2917, doi:10.1073/pnas.1702393115, 2018.

644 Mueller, K., Yadav, V., Lopez-Coto, I., Karion, A., Gourdji, S., Martin, C. and Whetstone, J.: Siting  
645 background towers to characterize incoming air for urban greenhouse gas estimation: a case study in the  
646 Washington DC/Baltimore Area, *J. Geophys. Res. Atmospheres*, 2017JD027364,  
647 doi:10.1002/2017JD027364, 2017.

648 Nemitz, E., Hargreaves, K. J., McDonald, A. G., Dorsey, J. R. and Fowler, D.: Micrometeorological  
649 Measurements of the Urban Heat Budget and CO<sub>2</sub> Emissions on a City Scale, *Environ. Sci. Technol.*,  
650 36(14), 3139–3146, doi:10.1021/es010277e, 2002.

651 Phillips, N. G., Ackley, R., Crosson, E. R., Down, A., Hutyra, L. R., Brondfield, M., Karr, J. D., Zhao, K.  
652 and Jackson, R. B.: Mapping urban pipeline leaks: Methane leaks across Boston, *Environ. Pollut.*,  
653 173(Supplement C), 1–4, doi:10.1016/j.envpol.2012.11.003, 2013.

654 Prussin, A. J., Marr, L. C., Schmale, D. G., Stoll, R. and Ross, S. D.: Experimental validation of a long-  
655 distance transport model for plant pathogens: Application to *Fusarium graminearum*, *Agric. For.*  
656 *Meteorol.*, 203, 118–130, doi:10.1016/j.agrformet.2014.12.009, 2015.

657 Rieker, G. B., Giorgetta, F. R., Swann, W. C., Kofler, J., Zolot, A. M., Sinclair, L. C., Baumann, E.,  
658 Cromer, C., Petron, G., Sweeney, C., Tans, P. P., Coddington, I. and Newbury, N. R.: Frequency-comb-  
659 based remote sensing of greenhouse gases over kilometer air paths, *Optica*, 1(5), 290–298,  
660 doi:10.1364/OPTICA.1.000290, 2014.

661 Rothman, L. S., Gordon, I. E., Barbe, A., Benner, D. C., Bernath, P. E., Birk, M., Boudon, V., Brown, L.  
662 R., Campargue, A., Champion, J. P., Chance, K., Coudert, L. H., Dana, V., Devi, V. M., Fally, S., Flaud,  
663 J. M., Gamache, R. R., Goldman, A., Jacquemart, D., Kleiner, I., Lacome, N., Lafferty, W. J., Mandin, J.  
664 Y., Massie, S. T., Mikhailenko, S. N., Miller, C. E., Moazzen-Ahmadi, N., Naumenko, O. V., Nikitin, A.  
665 V., Orphal, J., Perevalov, V. I., Perrin, A., Predoi-Cross, A., Rinsland, C. P., Rotger, M., Simeckova, M.,  
666 Smith, M. A. H., Sung, K., Tashkun, S. A., Tennyson, J., Toth, R. A., Vandaele, A. C. and Vander

667 Auwera, J.: The HITRAN 2008 molecular spectroscopic database, *J. Quant. Spectrosc. Radiat. Transf.*,  
 668 110(9–10), 533–572, doi:10.1016/j.jqsrt.2009.02.013, 2009.

669 Ryerson, T. B., Trainer, M., Holloway, J. S., Parrish, D. D., Huey, L. G., Sueper, D. T., Frost, G. J.,  
 670 Donnelly, S. G., Schauffler, S., Atlas, E. L., Kuster, W. C., Goldan, P. D., Hübler, G., Meagher, J. F. and  
 671 Fehsenfeld, F. C.: Observations of Ozone Formation in Power Plant Plumes and Implications for Ozone  
 672 Control Strategies, *Science*, 292(5517), 719–723, doi:10.1126/science.1058113, 2001.

673 Sargent, M., Barrera, Y., Nehrkorn, T., Hutyra, L. R., Gately, C. K., Jones, T., McKain, K., Sweeney, C.,  
 674 Hegarty, J., Hardiman, B., Wang, J. A. and Wofsy, S. C.: Anthropogenic and biogenic CO<sub>2</sub> fluxes in the  
 675 Boston urban region, *Proc. Natl. Acad. Sci.*, 115(29), 7491–7496, doi:10.1073/pnas.1803715115, 2018.

676 Seinfeld, J. H. and Pandis, S. N.: *Atmospheric Chemistry and Physics: From Air Pollution to Climate*  
 677 *Change*, Wiley., 2006.

678 Seto, K. C., Bigio, A., Bento, A., Cervero, R. and Christensen, P.: Human Settlements, Infrastructure, and  
 679 Spatial Planning, in *Climate Change 2014: Mitigation of Climate Change. Contribution of Working*  
 680 *Group III to the Fifth Assessment Report of the Intergovernmental Panel on Climate Change*, p. 78.,  
 681 2014.

682 Shusterman, A. A., Teige, V. E., Turner, A. J., Newman, C., Kim, J. and Cohen, R. C.: The BErkeley  
 683 Atmospheric CO<sub>2</sub> Observation Network: initial evaluation, *Atmos Chem Phys*, 16(21), 13449–13463,  
 684 doi:10.5194/acp-16-13449-2016, 2016.

685 Stauffer, J., Broquet, G., Bréon, F.-M., Puygrenier, V., Chevallier, F., Xueref-Rémy, I., Dieudonné, E.,  
 686 Lopez, M., Schmidt, M., Ramonet, M., Perrussel, O., Lac, C., Wu, L. and Ciais, P.: The first 1-year-long  
 687 estimate of the Paris region fossil fuel CO<sub>2</sub> emissions based on atmospheric inversion, *Atmos Chem Phys*,  
 688 16(22), 14703–14726, doi:10.5194/acp-16-14703-2016, 2016.

689 Truong, G.-W., Waxman, E. M., Cossel, K. C., Baumann, E., Klose, A., Giorgetta, F. R., Swann, W. C.,  
 690 Newbury, N. R. and Coddington, I.: Accurate frequency referencing for fieldable dual-comb  
 691 spectroscopy, *Opt. Express*, 24(26), 30495–30504, doi:10.1364/OE.24.030495, 2016.

692 Turnbull, J. C., Karion, A., Fischer, M. L., Faloona, I., Guilderson, T., Lehman, S. J., Miller, B. R.,  
 693 Miller, J. B., Montzka, S., Sherwood, T., Saripalli, S., Sweeney, C. and Tans, P. P.: Assessment of fossil  
 694 fuel carbon dioxide and other anthropogenic trace gas emissions from airborne measurements over  
 695 Sacramento, California in spring 2009, *Atmos Chem Phys*, 11(2), 705–721, doi:10.5194/acp-11-705-  
 696 2011, 2011.

697 Turner, D. B.: *Workbook of Atmospheric Dispersion Estimates*, [online] Available from:  
 698 [https://ia802704.us.archive.org/4/items/workbookofatmosp026353mbp/workbookofatmosp026353mbp.p](https://ia802704.us.archive.org/4/items/workbookofatmosp026353mbp/workbookofatmosp026353mbp.pdf)  
 699 [df](https://ia802704.us.archive.org/4/items/workbookofatmosp026353mbp/workbookofatmosp026353mbp.pdf) (Accessed 5 June 2017), 1970.

700 USA National Phenology Network. 2018. Plant and Animal Phenology Data. Data type: Site  
 701 Pheometrics. 09/01/2016-11/31/2016 for Region: Colorado. USA-NPN, Tucson, Arizona, USA. Data  
 702 set accessed 12/18/2018 at <http://doi.org/10.5066/F78S4N1>  
 703

704 Velasco, E., Pressley, S., Allwine, E., Westberg, H. and Lamb, B.: Measurements of CO<sub>2</sub> fluxes from the  
 705 Mexico City urban landscape, *Atmos. Environ.*, 39(38), 7433–7446, doi:10.1016/j.atmosenv.2005.08.038,  
 706 2005.

707 Velasco, E., Perrusquia, R., Jiménez, E., Hernández, F., Camacho, P., Rodríguez, S., Retama, A. and  
 708 Molina, L. T.: Sources and sinks of carbon dioxide in a neighborhood of Mexico City, *Atmos. Environ.*,  
 709 97(Supplement C), 226–238, doi:10.1016/j.atmosenv.2014.08.018, 2014.

710 Verhulst, K. R., Karion, A., Kim, J., Salameh, P. K., Keeling, R. F., Newman, S., Miller, J., Sloop, C.,  
 711 Pongetti, T., Rao, P., Wong, C., Hopkins, F. M., Yadav, V., Weiss, R. F., Duren, R. M. and Miller, C. E.:  
 712 Carbon dioxide and methane measurements from the Los Angeles Megacity Carbon Project – Part 1:  
 713 calibration, urban enhancements, and uncertainty estimates, *Atmos Chem Phys*, 17(13), 8313–8341,  
 714 doi:10.5194/acp-17-8313-2017, 2017.

715 Waxman, E. M., Cossel, K. C., Truong, G.-W., Giorgetta, F. R., Swann, W. C., Coburn, S., Wright, R. J.,  
 716 Rieker, G. B., Coddington, I. and Newbury, N. R.: Intercomparison of open-path trace gas measurements  
 717 with two dual-frequency-comb spectrometers, *Atmos Meas Tech*, 10(9), 3295–3311, doi:10.5194/amt-10-  
 718 3295-2017, 2017.

719 White, W. H., Anderson, J. A., Blumenthal, D. L., Husar, R. B., Gillani, N. V., Husar, J. D. and Wilson,  
 720 W. E.: Formation and transport of secondary air pollutants: ozone and aerosols in the St. Louis urban  
 721 plume, *Science*, 194(4261), 187–189, doi:10.1126/science.959846, 1976.

722 Wong, C. K., Pongetti, T. J., Oda, T., Rao, P., Gurney, K. R., Newman, S., Duren, R. M., Miller, C. E.,  
 723 Yung, Y. L. and Sander, S. P.: Monthly trends of methane emissions in Los Angeles from 2011 to 2015  
 724 inferred by CLARS-FTS observations, *Atmos Chem Phys*, 16(20), 13121–13130, doi:10.5194/acp-16-  
 725 13121-2016, 2016.

726 Wong, K. W., Fu, D., Pongetti, T. J., Newman, S., Kort, E. A., Duren, R., Hsu, Y.-K., Miller, C. E.,  
 727 Yung, Y. L. and Sander, S. P.: Mapping CH<sub>4</sub>: CO<sub>2</sub> ratios in Los Angeles with CLARS-FTS from Mount  
 728 Wilson, California, *Atmospheric Chem. Phys.*, 15(1), 241–252, doi:https://doi.org/10.5194/acp-15-241-  
 729 2015, 2015.

730 Wunch, D., Wennberg, P. O., Toon, G. C., Keppel-Aleks, G. and Yavin, Y. G.: Emissions of greenhouse  
 731 gases from a North American megacity, *Geophys. Res. Lett.*, 36(15), L15810,  
 732 doi:10.1029/2009GL039825, 2009.

733 Wunch, D., Toon, G. C., Sherlock, V., Deutscher, N. M., Liu, C., Feist, D. G. and Wennberg, P. O.:  
 734 Documentation for the 2014 TCCON Data Release, ,  
 735 doi:10.14291/tcon.ggg2014.documentation.r0/1221662, 2015.



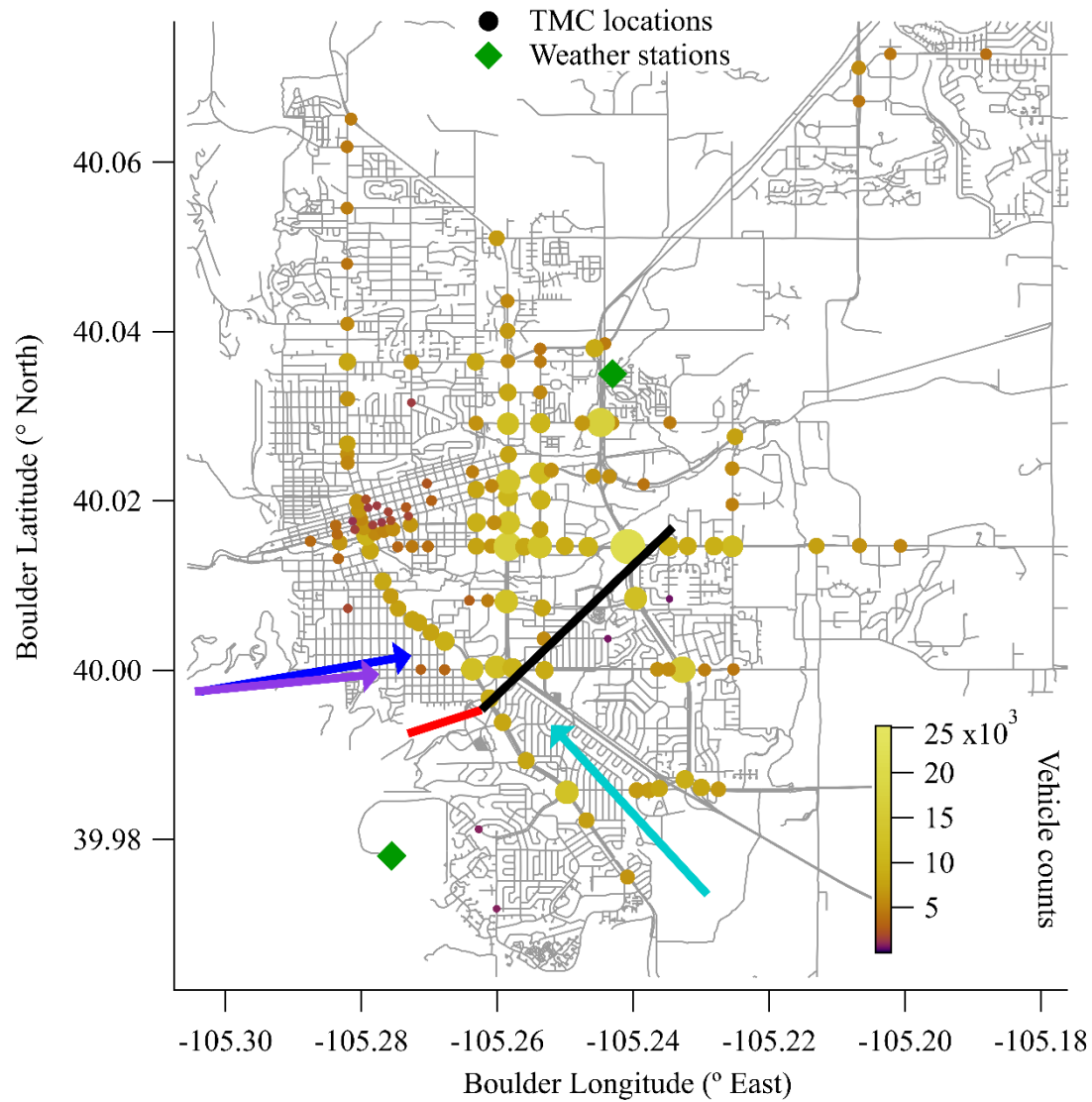


Figure 1: Measurement layout. The two measurement paths are shown by red (reference) and black (over-city) lines. The two weather stations that provided wind speed and direction data are given by the green diamonds. The colored circles are Turning Movement Count (TMC) locations, which are used as a proxy for the traffic source locations. Both color and size represent the number of traffic counts at each location. Dominant wind directions for the campaign overall (aqua) and the test case days (purple for 10/22 and blue for 10/25) are given by colored arrows.

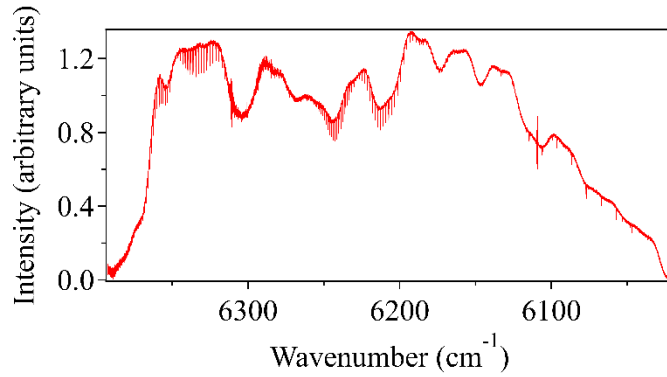


Figure 2: Typical 32-second spectrum measured over the 2-km reference path. CO<sub>2</sub> bands are observed in the 6350 cm<sup>-1</sup> and 6225 cm<sup>-1</sup> regions, while CH<sub>4</sub> and H<sub>2</sub>O are measured between 6150 and 6050 cm<sup>-1</sup>. The larger, slowly varying structure is from the comb intensity profile. The atmospheric absorption appears as the small and narrow dips.

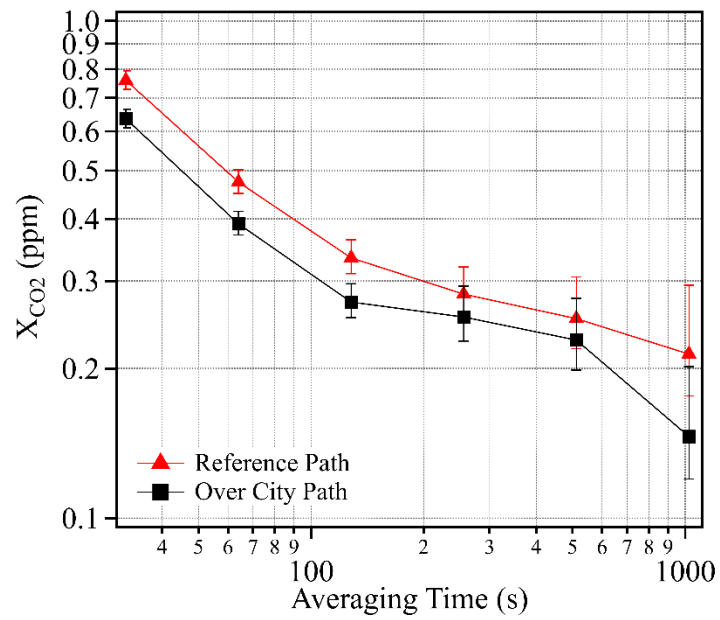


Figure 3: Statistical uncertainty as quantified by the Allan deviations for  $X_{CO_2}$  over both the reference path (red triangles) and city path (black squares) from a well-mixed, three-hour time period on the night of October 3, 2016.

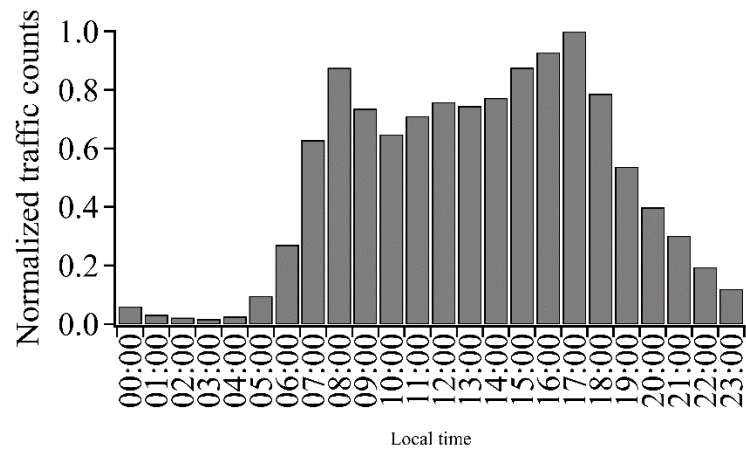


Figure 4: City-wide traffic counts from the Boulder Arterial Count Program (ART), normalized to a peak of unity.

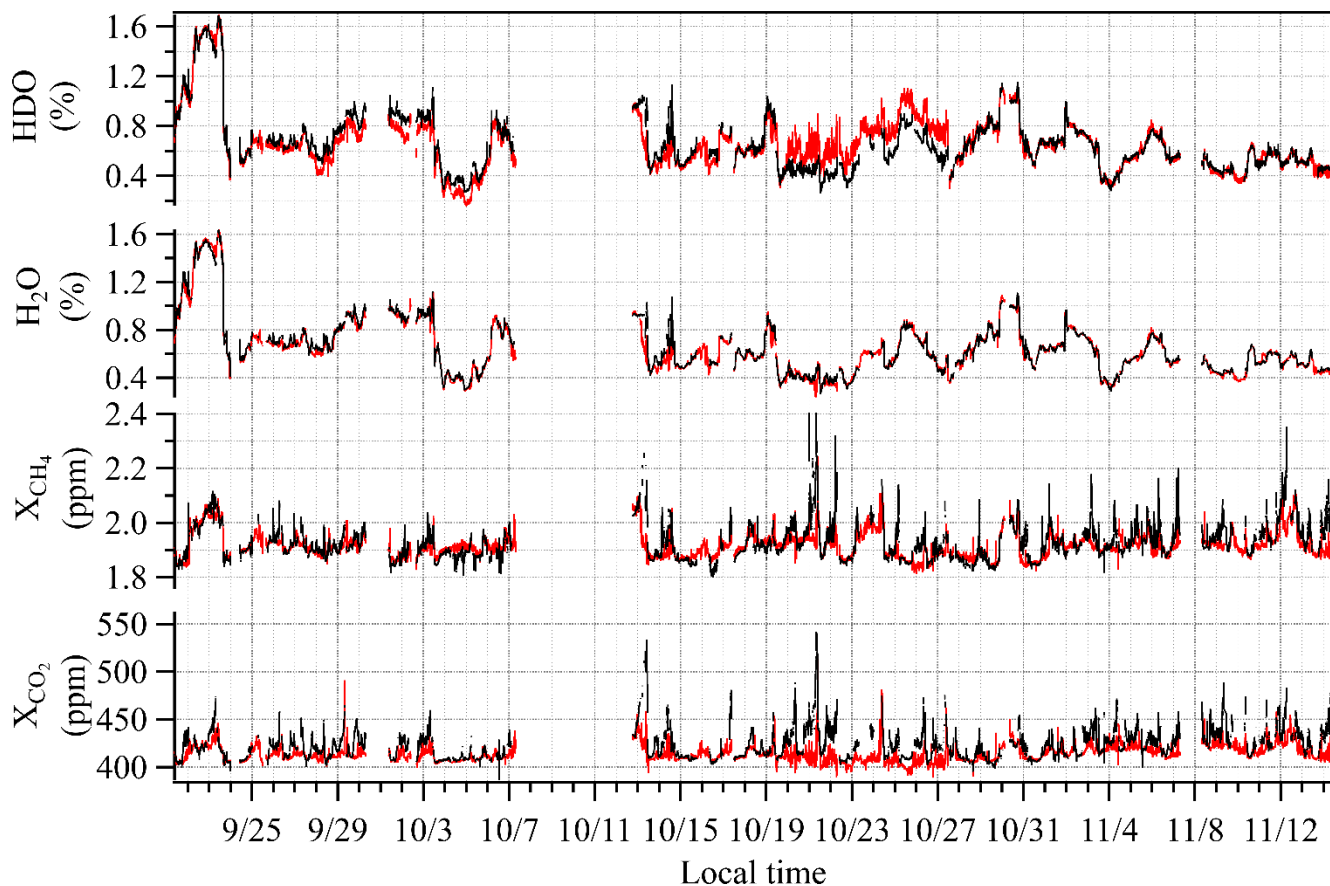


Figure 5: 7.5 weeks of dual-comb spectroscopy data for the reference path (red) and the over-city path (black) smoothed to 5-minute time intervals. Enhancements in the over-city path relative to the reference path are observed in CO<sub>2</sub> and CH<sub>4</sub> but not in H<sub>2</sub>O or HDO. (Note: the HDO concentration includes the HITRAN isotopic scaling.)

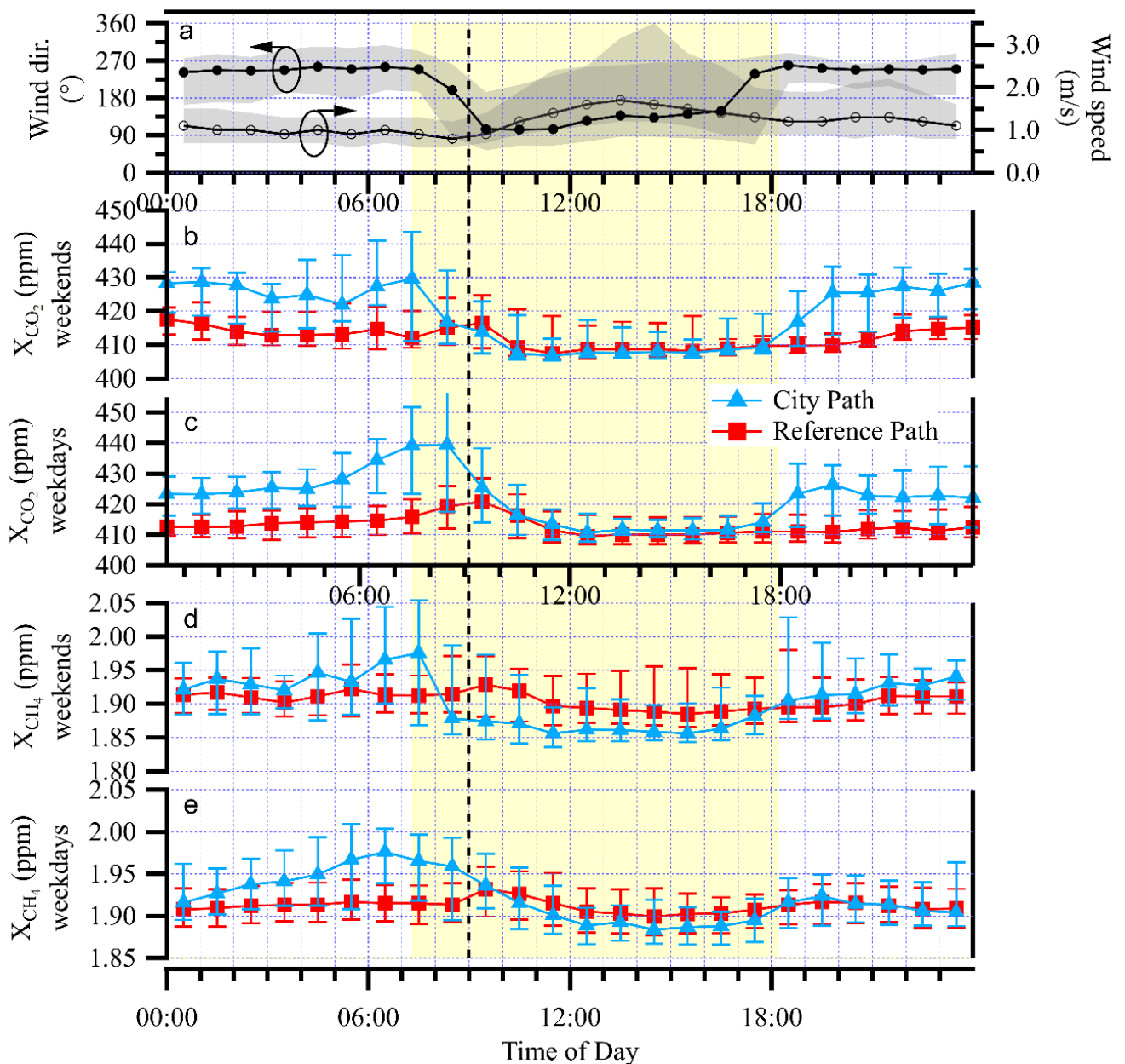


Figure 6: Diurnal cycle analysis. Data is the median of the full 7.5 weeks. (a) The mean direction in which the wind is blowing (black trace, left axis) and wind speed (gray trace, right axis) both from the NCAR Foothills measurement station, shaded regions reflect the 25<sup>th</sup> to 75<sup>th</sup> quartiles; (b) the weekend and (c) weekday median  $X_{CO_2}$  values for the over-city path (blue triangles) and reference path (red squares). Uncertainty bars represent the 25%-75% range of values encountered. (d) and (e) Same data for  $X_{CH_4}$ . The vertical dashed black line marks 9:00 local time and the yellow shaded region highlights the region from sunrise to sunset on Oct. 22, 2016.

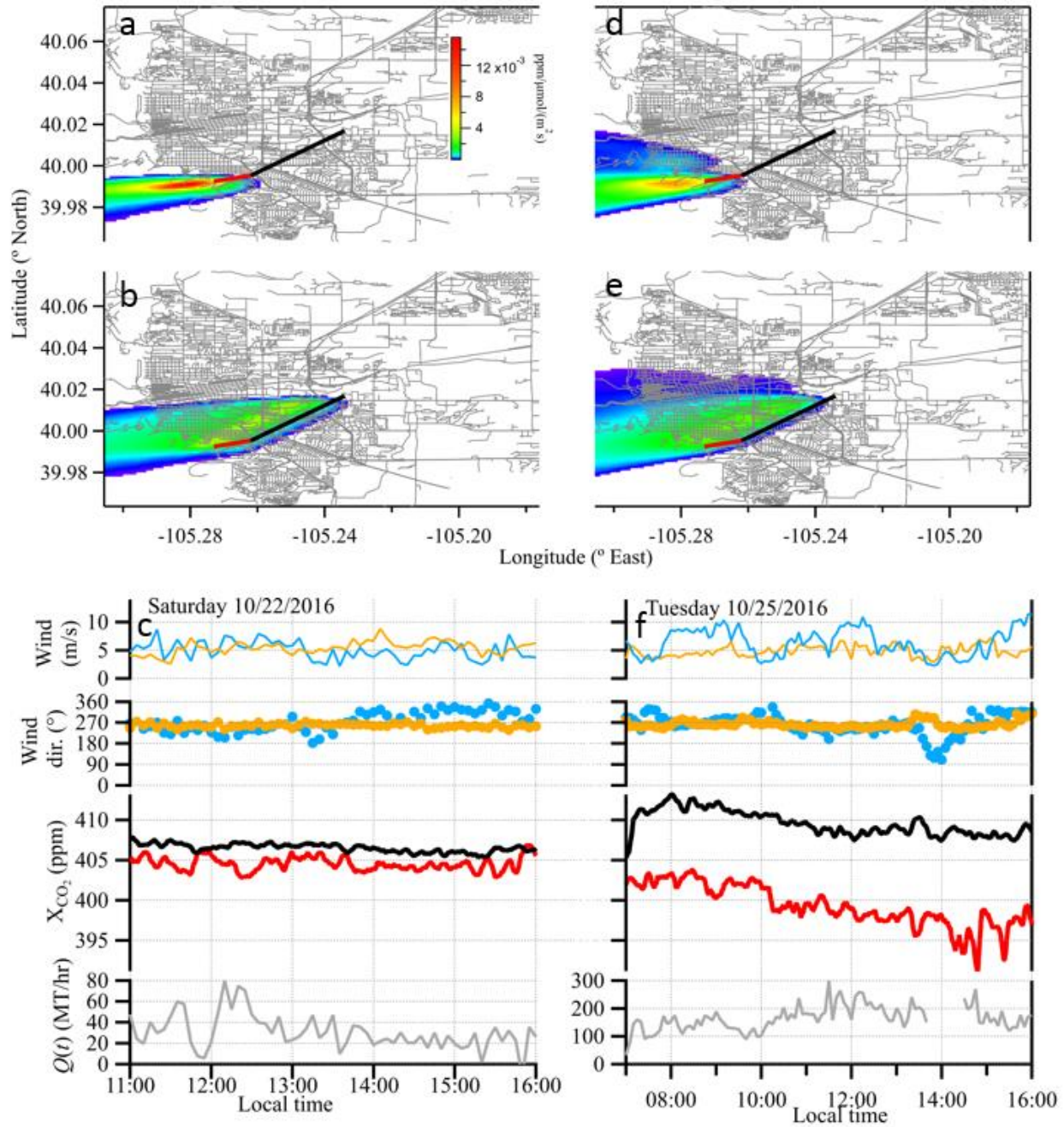


Figure 7: Footprint calculations and time series data for the two case study days. Left column: Saturday, October 22, 2016; right column: Tuesday, October 25, 2016 data. Upper panels (a, d): Footprints for the reference path. Middle panels (b, e): Footprints for the over-city path. The footprints are averaged over the respective time windows and open paths. Lower panels (c,f): Wind and CO<sub>2</sub> data at 5-minute time intervals. Reference and over-city measurement paths are shown in red and black, respectively. Data plots show X<sub>CO2</sub> over the reference path (red) and city path (black), wind speed and wind direction measurements taken at NCAR Mesa (blue) and NCAR Foothills (orange), and the calculated  $Q(t)$ . On Oct. 25,  $Q(t)$  data near 14:00 has been removed since the reference path wind direction is out of the southeast to east, resulting in city contamination along the reference path. All data is smoothed to 5-minute time intervals.

Table I: Parameters used to calculate the emission rate from Eq. (4). The measurement precision refers to the instrument uncertainty in the measurement quantity. The variability refers to the observed environmental variability over the measurement period. The variability from the enhancement, the wind direction, and the wind speed drive the observed variability in the estimated  $Q(t)$ . (The distance from a given source location to the DCS measurement path,  $\Delta x_j$ , varies with location and has a 5-m uncertainty.)

		10/22 11:00-16:00		10/25 7:00-16:00	
Quantity	Measurement precision	Mean	Variability	Mean	Variability
Pathlength $L$	0.15 m	6730.66 m	0	6730.66 m	0
Enhancement ( $c-c_0$ )	0.28 ppm (ref.) 0.25 ppm (city)	1.99 ppm	0.97 ppm (49%)	10.3 ppm	1.9 ppm (19%)
Wind speed $u$	0.3 m/s	5.2 m/s	1.0 m/s (19%)	5.6 m/s	1.3 m/s (23%)
Solar insolation	5%	570 W/m <sup>2</sup>	76 W/m <sup>2</sup> (13%)	275 W/m <sup>2</sup>	185 W/m <sup>2</sup> (67%)
Wind direction $\phi$	2°	265°	21°	264°	15°